CHINESE OPTICS LETTERS

Vol. 20, No. 8 | August 2022

Wideband Rydberg atom-based receiver for amplitude modulation radio frequency communication

Kai Yang (杨 凯), Zhanshan Sun (孙占山), Ruiqi Mao (毛瑞棋), Yi Lin (林 沂), Yi Liu (刘 燚), Qiang An (安 强)*, and Yunqi Fu (付云起)**

College of Electronic Science and Technology, National University of Defense Technology, Changsha 410073, China

*Corresponding author: anqiang18@nudt.edu.cn

**Corresponding author: yunqifu@nudt.edu.cn

Received January 19, 2022 | Accepted May 7, 2022 | Posted Online May 28, 2022

Based on Autler–Townes splitting and AC Stark shifts, we present a Rydberg atom-based receiver for determining the amplitude modulation (AM) frequency among a wideband carrier range utilizing a cesium atomic vapor cell. To verify this approach, we measured the signal-to-noise ratio and the data capacity with a 10 kHz AM frequency in the carrier range from 2 GHz to 18 GHz. Without changing the lasers, the working band can be easily extended to a higher range by optimizing the feed antenna and experimental configurations.

Keywords: Rydberg atoms; wideband; atomic receiver; amplitude modulation.

DOI: 10.3788/COL202220.081203

1. Introduction

Conventional radio frequency (RF) receivers acquire information by sensing electromagnetic waves at wavelengths comparable to their dimensions, so their corresponding bandwidth is limited by their physical size, according to the Chu limit[1]. Atomic receivers, on the other hand, hold great promise to overcome these constraints of classical sensors; in addition, they are non-invasive and are a truly satisfactory standard technology for sensing both *E*-field[2,3] and *H*-field[4,5] of external microwaves. Recent advances have been achieved by utilizing optical electromagnetically induced transparency (EIT) to excite individual alkali metal atoms to high-energy Rydberg states, which have large transition dipole moments (10^3–10^4 ea_0), making Rydberg atoms very sensitive to external RF waves[6]. To date, relying on on-resonance or near-resonance transitions between Rydberg states, the atomic receiver can respond in a wide range of frequencies [megahertz (MHz) to terahertz (THz)][7–9] and has the ability to measure the amplitude[10–12], polarization[13], phases[14,15], and angle[16] of the RF field. As such, several applications have been demonstrated, including electric field probe[17,18], stereo collector[19], spectrum analyzer[20,21], and digital communication signal receiver responding to amplitude modulated[22–24], frequency modulated[8,19,25], or phase modulated style[26]. Consequently, atom-based self-calibrating International System of Units (SI)-traceable quantum sensors have the potential to be the next generation of RF receivers.

However, most studies of atom-based receivers are on the basis of on-resonance transitions of Rydberg states at only a few individual frequencies[2,10–16] or some discontinuity working bands through varying the wavelength of the coupling laser[3,8,9]. Alternatively, by changing the frequency of the supporting RF field[21,27], these atomic receivers could respond to continuous frequencies with a certain bandwidth. The presence of secondary fields complicates the whole mechanism, and, on the other hand, in the near-resonance region, there is no exact relationship between the Stark shift and the target RF signal with the assistance of auxiliary fields. To the best of our knowledge, few studies have investigated continuous and broadband atom-based RF field sensors without altering the laser frequency or adding an RF field. To this end, a broadband atomic receiver is demonstrated in this Letter with no need to adjust the laser frequency or apply an external RF field.

2. Experimental Setup

The experimental setup and the Rydberg EIT ladder scheme as well as the resonant two-photon microwave transitions used in the measurements are illustrated in Fig. 1. The cesium (^{133}Cs) atoms were placed in a cylindrical glass vapor cell with a diameter of 1 mm and a length of 2 mm. The probe laser was tuned to 852 nm, with a focused $1/e^2$ beam diameter of 175 μm and a power of 4.72 μW into the vapor cell to excite the Cs atoms from the ground state ($|1\rangle$; $6S_{1/2}$, $F = 4$) to the intermediate state ($|2\rangle$; $6P_{3/2}$, $F' = 5$). Simultaneously, a 70.7 mW focused coupling laser with a $1/e^2$ beam diameter of 139 μm was tuned at 510 nm to excite the atoms from the intermediate state to the Rydberg state ($|3\rangle$; $42D_{5/2}$). The intensities of the probe and

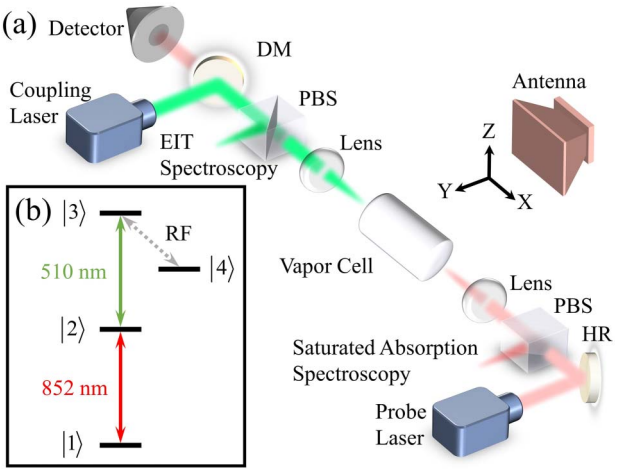

Fig. 1. Illustration of experimental scenarios and energy-level diagram. (a) Diagram of the experimental setup. DM, dichroic mirror; PBS, polarizing beam splitter; HR, dielectric mirror. (b) Energy-level diagram of the Rydberg EIT ladder scheme and resonant two-photon microwave transition.

coupling laser, which are counter-propagating and overlapped inside the center of vapor cell, were tuned to produce a high-contrast EIT signal to minimize Doppler broadening, and the absorption of the probe laser was monitored on a photodetector at room temperature. The RF field was generated by a signal generator with a maximum output power of 19 dBm and emitted by a horn antenna operating at 2–18 GHz. The antenna aperture is 79 cm × 84 cm, which was placed 160 cm in front of the vapor cell to satisfy the far-field condition, and the polarization was co-linear with both lasers. On this basis, we use the effective isotropic radiated power (EIRP) to specify the RF field strength at the vapor cell location, and EIRP can be expressed as $\mathrm{EIRP} = P_t + G_t - L_c$, where P_t is the signal generator output power, G_t is the feed antenna directional gain, and L_c is the cable loss between the signal generator and the feed antenna. Besides, to stabilize the laser frequency, two auxiliary Cs vapor cells were used in the experiment. The probe laser was stabilized on the saturated absorption spectral signal of the Cs D2 line. Similarly, the coupling laser can be stabilized by the EIT spectral signal generated by another vapor cell.

3. AT Splitting and AC Stark Shift

The Rydberg atom-based RF receivers can detect and measure broadband RF signals by using two related optical phenomena, the Autler–Townes (AT) splitting and the AC Stark shift. When a weak probe laser beam passes through a vapor cell filled with alkali metal gas, the probe laser is typically absorbed by the atoms, which may excite the atoms from the ground state to the intermediate state. Meanwhile, a relatively strong coupling laser causes the atoms to resonate between the intermediate and Rydberg states, inversely reducing the absorption of the probe laser and creating a transparent window of the probe laser, i.e., EIT. As an RF field is irradiated into the vapor cell, the EIT spectrum will be shifted, which is known as the AC Stark shift. In particular, when the frequency of the RF field allows atomic transition from one Rydberg state to another, the EIT spectrum will split into a pair of AT lines.

We calibrate the coupling laser detuning by taking advantage of the hyperfine structure, and typical EIT and AT splitting spectra are shown in Fig. 2(a). When the RF carrier frequency is tuned to 9.94 GHz, it resonates with the Rydberg state $|3\rangle$ and $|4\rangle$ ($43P_{3/2}$), resulting in a splitting of the EIT spectrum, as indicated by the red curve in Fig. 2(a). Moreover, the extent of the AT splitting Δ_{AT} is directly related to the RF field strength $|E|$:

$$\Delta_{\mathrm{AT}} = \frac{\mathcal{P}}{h}|E|, \tag{1}$$

where $\mathcal{P}$ is the atomic dipole moment, and h is Planck's constant. The EIT peak [black dash line in Fig. 2(a)] will vary with the RF field strength, which can be monitored by the

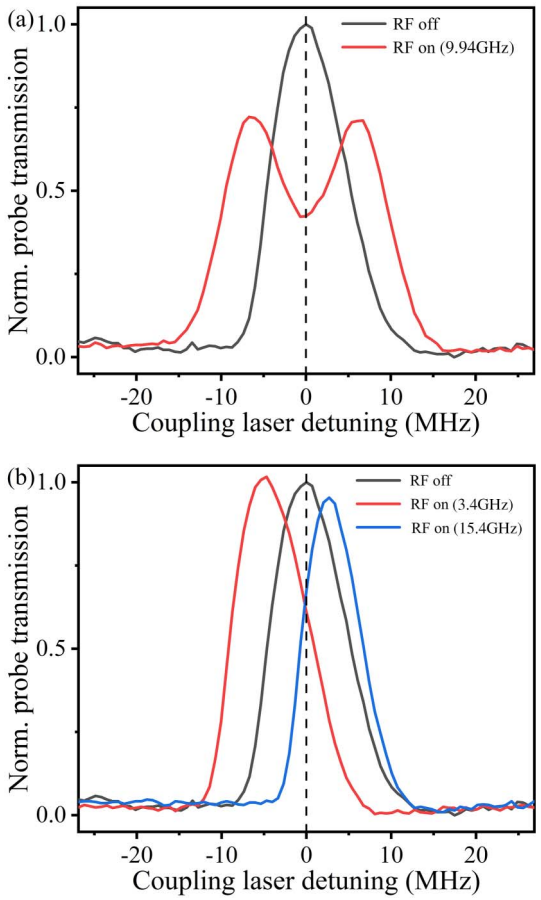

Fig. 2. Illustration of the normalized probe transmission signal as a function of coupling laser detuning. (a) On-resonance EIT spectra with (red curve) and without (black curve) RF field. The RF field frequency is 9.94 GHz. (b) Off-resonance EIT spectra with (red and blue curves) and without (black curve) RF field. The RF field frequencies are 3.4 GHz (red curve) and 15.4 GHz (blue curve).

photodetector. In contrast, by irradiating the RF field whose carrier frequencies are located in off-resonance regions, the induced EIT spectral signal will shift according to the AC Stark effect. Far from the resonant area, the Stark shift Δ_{Stark} of the target Rydberg state depends on the atomic polarizability $\alpha(\omega_{\text{RF}})$:

$$\Delta_{\text{Stark}} = -\frac{1}{2}\alpha(\omega_{\text{RF}})|E|^2. \tag{2}$$

The overall sign of Δ_{Stark} depends on whether the absolute energy of the Rydberg state coupled by the RF field is higher or lower than that of the optically probed Rydberg state. Specifically, the $\alpha(\omega_{\text{RF}})$ value is positive (negative) if the RF field frequency is lower (higher) than the resonant frequency. During the measurement in the frequency band of 2–18 GHz, the EIT signal will be red-shifted [red curve in Fig. 2(b)] by applying the RF field with a frequency lower than the resonant frequency, while it gets blue-shifted [blue curve in Fig. 2(b)] under the illumination of RF waves in higher bands. Hence, once the coupling laser frequency is locked to the peak of the EIT spectrum[28,29], the variation of the demodulated amplitude modulation (AM) signal can be read out on the photodetector in both on-resonance and off-resonance areas.

4. Experimental Results

For communication system applications, baseband bandwidth and signal-to-noise ratio (SNR) are critical metrics. Based on AT splitting, we characterize the response at different modulation depths for a carrier frequency of 9.94 GHz with an AM frequency of 10 kHz, as shown in Fig. 3. By setting the coupling laser frequency that corresponds to the peak of the EIT spectrum (Fig. 2), the changes of the RF field amplitude can be detected through the relative variations of the probe transmission on the photodetector, so the demodulated time domain signal waveform can be obtained using an oscilloscope, as shown in Fig. 3(a). It is obvious that the sinusoidal demodulated signal is amplified with the increase of the modulation depth from 10% to 60%. Figure 3(b) shows the frequency domain spectrum of the demodulated signal through a spectrum analyzer, determining an accurate 10 kHz AM frequency. The resolution bandwidth (RBW) of the spectrum analyzer was set to 1 Hz and was similarly set in the subsequent experiments.

According to Eqs. (1) and (2), the spectral variation is directly subjected to EIRP (EIRP $\propto |E|^2$), and this effect is ultimately exhibited as a positive correlation between the AM signal demodulated SNR and EIRP. In the on-resonance region, we demonstrated the atomic receiver's dynamic range by measuring the SNR of the demodulated signal as a function of the EIRP at 9.94 GHz, with an AM frequency of 10 kHz and a modulation depth of 60%, which is illustrated in Fig. 4. It is observed that the signal response is nearly linear over the EIRP from −15 dBm to 16 dBm, indicating a dynamic range over 31 dB. Beyond the linear region, the SNR gradually increases and reaches the peak value at about the EIRP of 27.3 dBm. After the peak, the SNR declines with the increase of the EIRP. The reason is that when

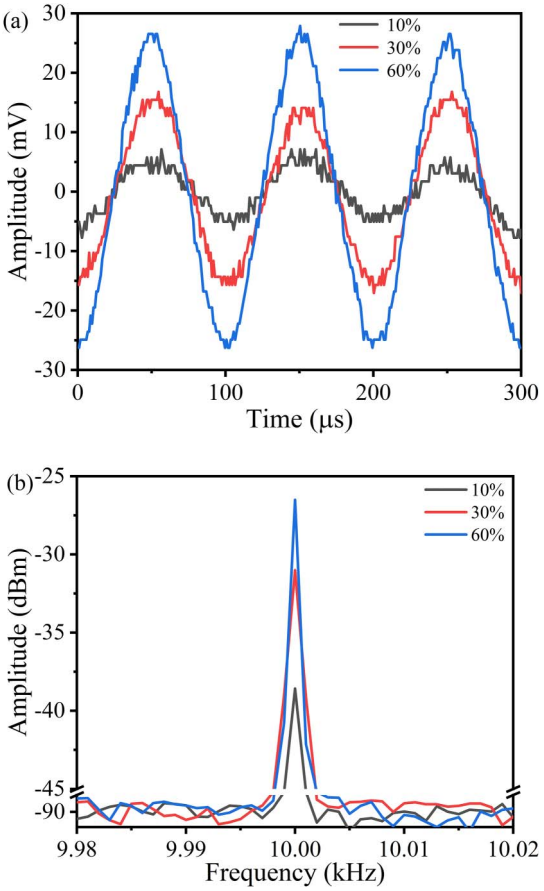

Fig. 3. Optical response measured at 9.94 GHz carrier frequency with an AM frequency of 10 kHz. AM depths are set to be 10% (black curve), 30% (red curve), and 60% (blue curve), respectively, and the EIRP is 26.3 dBm. (a) Oscilloscope output. (b) Spectrum analyzer output.

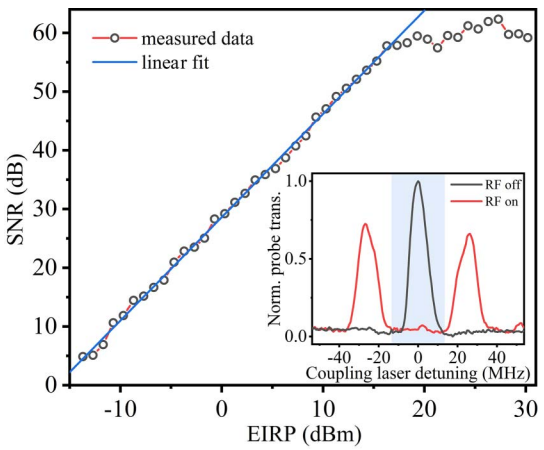

Fig. 4. Measured SNR of the demodulated signal as a function of the EIRP at the RF carrier frequency of 9.94 GHz with an AM frequency of 10 kHz and a modulation depth of 60%. Inset: typical EIT-AT spectra, when the EIRP is large enough to cause the splitting width to be larger than the EIT linewidth at an RF carrier frequency of 9.94 GHz.

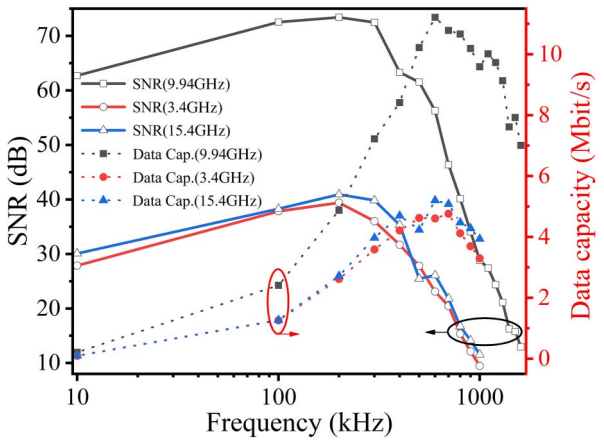

Fig. 5. Illumination of the SNR and data capacity as a function of AM frequency with a modulation depth of 60%. The RF carrier frequencies are 9.94 GHz (black, square) with an EIRP of 26.3 dBm, 3.4 GHz (red, circle) with an EIRP of 26 dBm, and 15.4 GHz (blue, triangle) with an EIRP of 29.8 dBm, respectively. The hollow symbols represent the experimental data of the SNR, and the solid symbols represent the data capacity calculated by Eq. (3).

the EIRP keeps increasing, the AT pair will be separated far from the initial EIT peak, and thus the locked point on the output signal falls to the background noise area and fails to efficiently reflect the AM envelope.

The data capacity, which can be described in bits per second, is also one of the most important characteristics in communication systems. Based on the Shannon–Hartley theorem[30], the data capacity can be described as $C = \mathrm{BW} \times \log_2(1 + \mathrm{SNR})$, where BW is the channel bandwidth. Differently, according to Refs. [23,24], the achievable data capacity C for the atomic reception mechanism can be indicated as

$$C = f_{\mathrm{AM}} \times \log_2(1 + \mathrm{SNR}_{N=1}), \tag{3}$$

where f_{AM} is the given AM frequency. By varying the frequency of the signal generator, three representative frequency points in the on-resonance (9.94 GHz) and two-sided off-resonance (3.4 GHz and 15.4 GHz) regions with a modulation depth of 60% are irradiated to the vapor cell one by one. Figure 5 illustrates the variation of SNR and data capacity as a function of AM frequency under different RF carrier frequencies. It can be obviously seen that the SNR and the corresponding data capacity in the on-resonance region is larger than those in the off-resonance region, due to the fact that in the on-resonance region, where the atoms are more sensitive to the RF-induced changes than in the off-resonance regions, the output signal of the photodetector has a larger margin to reflect the variation of the AM signal. As expected, the SNR progressively deteriorates with the increase of AM frequency. This is because the dynamic time for a steady EIT to build up again, which can be characterized by the inverse of the dephasing rate, is inevitably worsened by many factors, such as collisional relaxation, spontaneous emission, transit time broadening, and so forth. In our experiment, the maximum detectable AM frequency is over 1.6 MHz. The data capacity shows a near linear dependence on AM frequencies less than 300 kHz, rising to peaks with a tapering increase from 300 kHz to 700 kHz of the AM frequencies. After that, it begins to decline on account of the declension of SNR. We found that the maximum data capacity of our atomic receiver is obtained in the on-resonance region, which is about 11.2 Mbit/s. Moreover, the data capacity in the blue off-resonance region (~5.2 Mbit/s at 15.4 GHz) is slightly bigger than that in the red off-resonance region (~4.7 Mbit/s at 3.4 GHz), which might be related to the signal strength at different carrier frequencies.

To verify the broadband characteristics of our atomic receiver, we measured the SNR and its corresponding EIRP throughout an ultra-wideband ranging from 2 GHz to 18 GHz, which is restricted by the limited operating band of the antenna used in the experiment. The AM frequency is fixed at 10 kHz with the modulation depth of 60%. The measured SNR and its corresponding EIRP are illustrated in Fig. 6. For the overall trend, it is worth noting that the SNR reaches a maximum near the on-resonance region (10 GHz) and decreases in off-resonance regions, which corresponds to the sensitivity of the atoms to the external RF field in different regions. According to Eq. (2), the Rydberg EIT spectrum is governed by the atomic polarizability $\alpha(\omega_{\mathrm{RF}})$ that varies with RF field frequency, and the value of the $\alpha(\omega_{\mathrm{RF}})$ in the resonant region is much larger than that in the off-resonance regions. As a result, the demodulated AM signal SNR obtains its maximum in the resonant region and gradually decreases as the RF field frequency slowly moves away from the resonant frequency. In addition, the fluctuation of the EIRP ($\mathrm{EIRP} \propto |E|^2$) also has impact on the SNR, but its influence is negligible compared to that of $\alpha(\omega_{\mathrm{RF}})$. What is more, the SNR dithers in the broadband carrier frequency range, which might be attributed to environmental scattering during the measurements. In particular, there is a small peak in the SNR at a carrier frequency of 17 GHz. This is because the responding carrier wavelength is 1.76 cm and comparable to the length of the

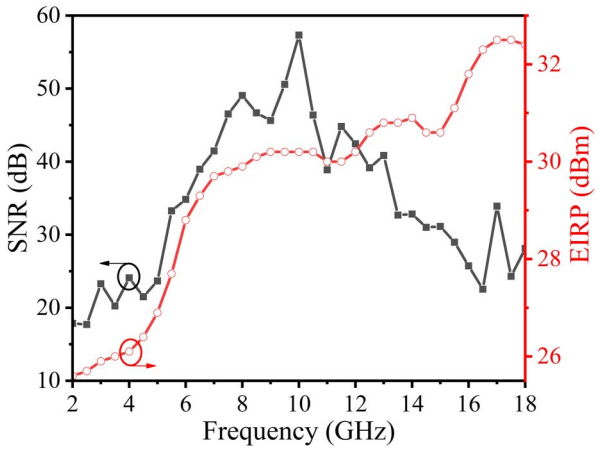

Fig. 6. Illumination of the measured SNR (black) and corresponding EIRP (red) as a function of the RF carrier frequency with an AM frequency of 10 kHz and a modulation depth of 60%.

vapor cell (considering a wall thickness of 1 mm on both sides), where the standing wave was formed in the laser action area and further enhanced the *E*-field amplitude. The results demonstrate that our atomic sensor has the capability to detect broadband and continuous electromagnetic waves without changing the laser frequency or auxiliary devices; furthermore, the SNR can be subsequently improved by increasing the illuminated power in off-resonance regions.

5. Conclusion

This paper demonstrated a Rydberg atom-based RF sensor for proof-of-concept AM communications, operating at an ultra-wideband carrier frequency from 2 GHz to 18 GHz, without changing the laser wavelength or applying other auxiliary RF fields, which makes the quantum receiver more robust and more maintainable in practical applications. The measured bandwidth, which is mainly restricted by the antenna working band and related instruments, can be easily extended to a broader frequency range by optimizing the experimental conditions. Through locking the coupling laser frequency at the peak of the EIT spectrum, the atomic receiver can demodulate the amplitude variation of the scattered RF field based on off-resonance AC Stark shift and on-resonance AT splitting effects. We characterized the SNR and its corresponding data capacity from 2 GHz to 18 GHz, exhibiting the distinguished sensing ability spanning the prime microwave communication bands. The quantum sensor proposed in our study will be a complimentary candidate for future communication domains.

Acknowledgement

This work was supported by the National Natural Science Foundation of China (Nos. 12104509 and 61901495).

References

1. L. J. Chu, "Physical limitations of omni-directional antennas," J. Appl. Phys. **19**, 1163 (1948).
2. J. A. Sedlacek, A. Schwettmann, H. Kübler, R. Löw, T. Pfau, and J. P. Shaffer, "Microwave electrometry with Rydberg atoms in a vapour cell using bright atomic resonances," Nat. Phys. **8**, 819 (2012).
3. C. L. Holloway, J. A. Gordon, S. Jefferts, A. Schwarzkopf, D. A. Anderson, S. A. Miller, N. Thaicharoen, and G. Raithel, "Broadband Rydberg atom-based electric-field probe: from self-calibrated measurements to sub-wavelength imaging," IEEE Trans. Antenna Propag. **62**, 6169 (2014).
4. P. Böhi, M. F. Riedel, T. W. Hänsch, and P. Treutlein, "Imaging of microwave fields using ultracold atoms," Appl. Phys. Lett. **97**, 051101 (2010).
5. P. Böhi and P. Treutlein, "Simple microwave field imaging technique using hot atomic vapor cells," Appl. Phys. Lett. **101**, 181107 (2012).
6. A. K. Mohapatra, T. R. Jackson, and C. S. Adams, "Coherent optical detection of highly excited Rydberg states using electromagnetically induced transparency," Phys. Rev. Lett. **98**, 113003 (2007).
7. Y. Y. Jau and T. Carter, "Vapor-cell-based atomic electrometry for detection frequencies below 1 kHz," Phys. Rev. Appl. **13**, 054034 (2020).
8. D. A. Anderson, R. E. Sapiro, and G. Raithel, "An atomic receiver for AM and FM radio communication," IEEE Trans. Antenna Propag. **69**, 2455 (2021).
9. D. A. Anderson, E. Paradis, G. Raithel, R. E. Sapiro, and C. L. Holloway, "High-resolution antenna near-field imaging and sub-THz measurements with a small atomic vapor-cell sensing element," in *11th Global Symposium on Millimeter Waves (GSMM)* (2018), p. 1.
10. M. Y. Jing, Y. Hu, J. Ma, H. Zhang, L. J. Zhang, L. T. Xiao, and S. T. Jia, "Atomic superheterodyne receiver based on microwave-dressed Rydberg spectroscopy," Nat. Phys. **16**, 911 (2020).
11. C. L. Holloway, M. T. Simons, M. D. Kautz, A. H. Haddab, J. A. Gordon, and T. P. Crowley, "A quantum-based power standard: using Rydberg atoms for a SI-traceable radio-frequency power measurement technique in rectangular waveguides," Appl. Phys. Lett. **113**, 094101 (2018).
12. M. T. Simons, J. A. Gordon, C. L. Holloway, D. A. Anderson, S. A. Miller, and G. Raithel, "Using frequency detuning to improve the sensitivity of electric field measurements via electromagnetically induced transparency and Autler-Townes splitting in Rydberg atoms," Appl. Phys. Lett. **108**, 174101 (2016).
13. J. A. Sedlacek, A. Schwettmann, H. Kübler, and J. P. Shaffer, "Atom-based vector microwave electrometry using rubidium Rydberg atoms in a vapor cell," Phys. Rev. Lett. **111**, 063001 (2013).
14. M. T. Simons, A. H. Haddab, J. A. Gordon, and C. L. Holloway, "A Rydberg atom-based mixer: measuring the phase of a radio frequency wave," Appl. Phys. Lett. **114**, 114101 (2019).
15. D. A. Anderson, R. E. Sapiro, L. F. Gonçalves, R. Cardman, and G. Raithel, "Atom radio-frequency interferometry," arXiv:2010.13657 (2020).
16. A. K. Robinson, N. Prajapati, D. Senic, M. T. Simons, and C. L. Holloway, "Determining the angle-of-arrival of a radio-frequency source with a Rydberg atom-based sensor," Appl. Phys. Lett. **118**, 114001 (2021).
17. M. T. Simons, J. A. Gordon, and C. L. Holloway, "Fiber-coupled vapor cell for a portable Rydberg atom-based radio frequency electric field sensor," Appl. Opt. **57**, 6456 (2018).
18. R. Cardman, L. F. Gonçalves, R. E. Sapiro, G. Raithel, and D. A. Anderson, "Atomic 2D electric field imaging of a Yagi–Uda antenna near-field using a portable Rydberg-atom probe and measurement instrument," Adv. Opt. Tech. **9**, 305 (2020).
19. C. L. Holloway, M. T. Simons, A. H. Haddab, J. A. Gordon, and S. D. Voran, "A multiple-band Rydberg atom-based receiver: AM/FM stereo reception," IEEE Antennas Propag. Mag. **63**, 63 (2021).
20. D. H. Meyer, Z. A. Castillo, K. C. Cox, and P. D. Kunz, "Assessment of Rydberg atoms for wideband electric field sensing," J. Phys. B: At. Mol. Opt. Phys. **53**, 034001 (2020).
21. D. H. Meyer, P. D. Kunz, and K. C. Cox, "Waveguide-coupled Rydberg spectrum analyzer from 0 to 20 GHz," Phys. Rev. Appl. **15**, 014053 (2021).
22. D. H. Meyer, K. C. Cox, F. K. Fatemi, and P. D. Kunz, "Digital communication with Rydberg atoms and amplitude-modulated microwave fields," Appl. Phys. Lett. **112**, 211108 (2018).
23. K. C. Cox, D. H. Meyer, F. K. Fatemi, and P. D. Kunz, "Quantum-limited atomic receiver in the electrically small regime," Phys. Rev. Lett. **121**, 110502 (2018).
24. J. S. Otto, M. K. Hunter, N. Kjærgaard, and A. B. Deb, "Data capacity scaling of a distributed Rydberg atomic receiver array," J. Appl. Phys. **129**, 154503 (2021).
25. H. Y. Zou, Z. F. Song, H. H. Mu, Z. G. Feng, J. F. Qu, and Q. L. Wang, "Atomic receiver by utilizing multiple radio-frequency coupling at Rydberg states of rubidium," Appl. Sci. **10**, 1346 (2020).
26. C. L. Holloway, M. T. Simons, J. A. Gordon, and D. Novotny, "Detecting and receiving phase-modulated signals with a Rydberg atom-based receiver," IEEE Antennas Wirel. Propag. Lett. **18**, 1853 (2019).
27. M. T. Simons, A. B. Artusio-Glimpse, C. L. Holloway, E. Imhof, S. R. Jefferts, R. Wyllie, B. C. Sawyer, and T. G. Walker, "Continuous radio-frequency electric-field detection through adjacent Rydberg resonance tuning," Phys. Rev. A **104**, 032824 (2021).
28. Y. Sun, Y. Yao, Y. Q. Hao, H. F. Yu, Y. Y. Jiang, and L. S. Ma, "Laser stabilizing to ytterbium clock transition with Rabi and Ramsey spectroscopy," Chin. Opt. Lett. **18**, 070201 (2020).
29. X. T. Chen, Y. Y. Jiang, B. Li, H. F. Yu, H. F. Jiang, T. Wang, Y. Yao, and L. S. Ma, "Laser frequency instability of 6×10^{-16} using 10-cm-long cavities on a cubic spacer," Chin. Opt. Lett. **18**, 030201 (2020).
30. C. E. Shannon, "Communication in the presence of noise," Proc. IRE **37**, 10 (1949).